

Assessment of arterial characteristics in human atherosclerosis by extracting optical properties from polarization-sensitive optical coherence tomography

Wen-Chuan Kuo,^{1,*} Ming-Wei Hsiung,¹ Jeou-Jong Shyu,² Nai-Kuan Chou,³
and Po-Nien Yang¹

¹ Institute of Electro-optical Science and Technology, National Taiwan Normal University, 88, Sec. 4, Ting-Chou Road, Taipei 116, Taiwan

² Department of Veterinary Medicine, National Taiwan University, Taipei 106, Taiwan

³ Department of the Surgery, National Taiwan University Hospital, Taipei 100, Taiwan

*Corresponding author: kwchuan@ntnu.edu.tw

Abstract: In this research, we assessed arterial characteristics in human atherosclerosis by determining both scattering and birefringence properties of vessel tissue from polarization-sensitive optical coherence tomography (PS-OCT) images. We demonstrated that optical characteristics including scattering coefficient (μ_s), effective anisotropy factor (g_{eff}), birefringence coefficient (Δn), and fast-axis angle (β) of normal and different kinds of atherosclerotic lesions in human vessels can be quantitatively described. Based on our findings, a quantitative PS-OCT image criterion for plaque characterization was constructed.

©2008 Optical Society of America

OCIS codes: (260.5430) Polarization, (170.4500) Optical coherence tomography, (170.4580) optical diagnostics for medicine.

References and links

1. D. Huang, E. A. Swanson, C. P. Lin, J. S. Schuman, W. G. Stinson, W. Chang, M. R. Hee, T. Flotte, K. Gregory, C. A. Puffalito, and J. G. Fujimoto, "Optical coherence tomography," *Science* **254**, 1178–1181 (1991).
2. M. E. Brezinski, G. J. Tearney, B. E. Bouma, J. A. Izatt, M. R. Hee, E. A. Swanson, J. F. Southern, and J. G. Fujimoto, "Optical coherence tomography for optical biopsy: properties and demonstration of vascular pathology," *Circulation* **93**, 1206–1213 (1996).
3. J. G. Fujimoto, M. E. Bresinski, G. J. Tearney, S. A. Boppart, B. E. Bouma, M. R. Hee, J. F. Southern, and E. A. Swanson, "Optical biopsy and imaging using optical coherence tomography," *Nat. Med.* **1**, 970-972 (1995).
4. M. E. Bresinski, G. J. Tearney, N. J. Weissman, S. A. Boppart, B. E. Bouma, M. R. Hee, A. E. Weyman, E. A. Swanson, J. F. Southern, and J. G. Fujimoto, "Assessing atherosclerotic plaque morphology: comparison of optical coherence tomography and high frequency intravascular ultrasound," *Heart* **77**, 397-403 (1997).
5. H. Yabushita, B. E. Bouma, S. L. Houser, H. T. Aretz, I. K. Jang, K. H. Schlendorf, C. R. Kauffman, M. Shishkov, D. H. Kang, E. F. Halpern, and G. J. Tearney, "Characterization of human atherosclerosis by optical coherence tomography," *Circulation* **106**, 1640–1645 (2002).
6. I. K. Jang, B. E. Bouma, D. H. Kang, S. J. Park, S. W. Park, K. B. Seung, K. B. Choi, M. Shishkov, K. Schlendorf, E. Pomerantsev, S. L. Houser, H. T. Aretz, and G. J. Tearney, "Visualization of coronary atherosclerotic plaques in patients using optical coherence tomography: comparison with intravascular ultrasound," *J. Am. Coll. Cardiol.* **39**, 604–609 (2002).
7. D. Stamper, N. J. Weissman, M. Brezinski, "Plaque characterization with optical coherence tomography," *J. Am. Coll. Cardiol.* **47**, C69–C79 (2006).
8. G. J. Tearney, I-K Jang, B. E. Bouma, "Optical coherence tomography for imaging the vulnerable plaque," *J. Biomed. Opt.* **11**, 021002 (2006).
9. G. J. Tearney, H. Yabushita, S. L. Houser, H. T. Aretz, I. K. Janf, K. H. Schlendorf, C. R. Kauffman, M. Shishkov, E. F. Halpern, and B. E. Bouma, "Quantification of macrophage content in atherosclerotic plaques by optical coherence tomography," *Circulation* **107**, 113–119 (2003).
10. W. C. Kuo, J. J. Shyu, N. K. Chou, C. M. Lai, H. C. Huang, C. Chou, G. J. Jan, "Imaging of Human Aortic Atherosclerotic plaques by Polarization-Sensitive Optical Coherence Tomography," in *Proceedings of IEEE Conference on Engineering in Medicine and Biology* (San Francisco, 2004), pp. 1111-1114.

11. W. C. Kuo, J. J. Shyu, N. K. Chou, C. M. Lai, E. K. Tien, H. J. Huang, C. Chou, and G. J. Jan, "Correlation of collagen synthesis with polarization-sensitive optical coherence tomography imaging of *in vitro* human atherosclerosis," *Proc. SPIE* **5690**, 563-571 (2005).
12. S. D. Giattina, B. K. Courtney, P. R. Herz, M. Harman, S. Shortkroff, D. L. Stamper, B. Liu, J. G. Fujimoto, M. E. Brezinski, "Assessment of coronary plaque collagen with polarization sensitive optical coherence tomography (PS-OCT)," *Int. J. Cardiol.* **107**, 400-409 (2006).
13. S. K. Nadkarni, M. C. Pierce, B. H. Park, J. F. de Boer, P. Whittaker, B. E. Bouma, J. E. Bressner, E. Halpern, S. L. Houser, and G. J. Teaney, "Measurement of collagen and smooth muscle cell content in atherosclerotic plaques using polarization sensitive optical coherence tomography," *J. Am. Coll. Cardiol.* **49**, 1474-1481 (2007).
14. W. C. Kuo, N. K. Chou, C. Chou, C. M. Lai, H. J. Huang, and J. J. Shyu, "Polarization-sensitive optical coherence tomography for imaging human atherosclerosis," *Appl. Opt.*, **46**, 2520-2527 (2007).
15. W. C. Kuo, M. W. Hsiung, and P. N. Yang, "Extracting quantitative optical properties of human vessel from PS-OCT images," *Med. Biol. Eng.* **27**, 191-197 (2007).
16. W. C. Kuo, M. W. Hsiung, J. J. Shyu, N. K. Chou, and P. N. Yang, "Quantitative analysis on optical properties of human atherosclerosis by using polarization-sensitive optical coherence tomography," *Proc. SPIE* **6842**, 684223-1~6842323-9 (2008).
17. L. Thrane, H. T. Yura, and P. E. Andersen, "Analysis of optical coherence tomography systems based on the extended Huygens-Fresnel principle," *J. Opt. Soc. Am. A* **17**, 484-490 (2000).
18. D. Levitz, L. Thrane, M. H. Frosz, P. E. Andersen, C. B. Andersen, J. Valanciunaite, J. Swartling, S. Andersson-Engels and P. R. Hansen, "Determination of optical properties of highly-scattering media in optical coherence tomography," *Opt. Express* **12**, 249-259 (2004).
19. C. E. Metz, "Basic principles of ROC analysis," *Semin. Nucl. Med.* **8**, 283-298 (1978).

1. Introduction

Optical coherence tomography (OCT), based on a low-coherence interferometer, has emerged as a rapid, non-contact and noninvasive, high-resolution imaging tool [1]. From the mid-1990s, the ability of OCT to successfully perform micron scale imaging of both *in vitro* human aorta and coronary arteries was demonstrated [2,3]. The axial resolution of OCT is capable of resolving small structural details, such as the presence of fissures of atherosclerotic plaques [2]. Since the rupture of atherosclerotic plaques is the most common event initiating acute ischemic heart disease, the objective OCT image criterion for risk-stratifying plaque characterization has been established on the basis of the intrinsic optical properties of typical plaque, whose constituents are lipid, calcium, or fibrous tissue [4-8]. Activated macrophages which impede collagen synthesis leading to plaque instability have also been quantified by the standard deviation of the OCT signal intensity [9]. However, as plaque components are heterogeneous, they may sometimes generate reflected signals that confuse or obscure the identity of these components; multiple scattering by the cap also creates difficulty in identifying plaque by the diffuse nature of the plaque border [7].

In 2004, we presented the application of PS-OCT in human atherosclerosis, and proposed an alternative approach to characterize a plaque lesion based on its birefringence property [10]. Specimen birefringence characterizes the differential speed of propagation between two orthogonal polarized states of light, which is also a direct result of the existence of more than one index of refraction. We demonstrated that the normal vascular intima has a low intrinsic birefringence property, while the classic atheroma (due to the accumulation of collagen) has a strong PS-OCT signal (i.e., a large amount of phase retardation) [11]. Assessing the phase retardation change may quantify the collagen content in atherosclerotic lesions. It may provide significant pathophysiological information, and influence clinical decision-making in patients with risk factors. Recently, identifying organized collagen in arteries has also been demonstrated by using single detector PS-OCT [12]. In addition, another report showed PS-OCT measurements of birefringence have a strong positive correlation with thick collagen fiber content ($r=0.76$, $p<0.001$) and also smooth muscle cells density ($r=0.74$, $p<0.01$) [13].

In a recent study [14], we found that marked PS-OCT signal change can be seen not only in fibroatheroma, but also in calcified plaque. In addition, different orientations of fast-axis angle of PS-OCT images in some parts of the calcified plaques may indicate different structural orientations. Therefore, the current study extracted scattering coefficient (μ_s) and effective anisotropy factor (g_{eff}) from the intensity image of PS-OCT (the same as OCT image). The birefringence coefficient (Δn) and the fast-axis angle (β) were defined by

detecting the change in the polarization state of the incident light of the PS-OCT system. The significant difference of these quantified optical properties in different types of human vessels was analyzed. The correlation between these four optical variables was also evaluated. Whether change in these quantified optical properties could be used to construct a plaque characterization criterion was examined.

2. Materials and methods

Specimens of the aorta with white or yellow plaque were obtained from heart transplant recipients at the National Taiwan University Hospital, Taiwan. The protocol was approved by the ethics committees of National Taiwan University Hospital. The PS-OCT setup used in this study has been described in detail previously [14]. The specimens were dipped in saline (4°C), cut into segments smaller than 1 x 1 cm, and examined. The segment was mounted in a cuvette and moistened with normal saline bath maintained at 37 °C during imaging. Over 25 segments, each containing different amounts of plaque, were used. The intimal surface was exposed for PS-OCT imaging. Three images (reflectivity R, phase retardation Φ , and fast-axis angle β) were acquired simultaneously, based on the amplitude and phase of the interference signal. An algorithm was then used to determine the four quantitative optical properties from the above three images [15, 16]. First, the user selected regions (ex. white rectangle in the left column of Fig. 1) corresponding to those evaluated by histopathology from different area of the images. Regions were then automatically divided into several ROIs (ex. green dashed inset in the left column of Fig. 1) spanning from the intimal surface and approximately including 25 A-scans. Also the size in each ROI should be kept constant. After laterally (i.e. along the x-axis) delineating and averaging the R, Φ , and β signals within each ROI, the μ_s and root-mean-square scattering angle (θ_{rms}), which can be used to calculate the effective anisotropy factor ($g_{eff} = \cos(\theta_{rms})$), were extracted by fitting the reflectivity signals as a function of depth to an extended Huygens-Fresnel model [15-18] as represented in the right column of Fig. 1.

$$\langle i^2(z) \rangle = \left\{ \frac{\alpha^2 P_R P_S \sigma_b}{\pi \omega_H^2} \right\} \cdot \left\{ \exp(-2\mu_s z) + \frac{4\exp(-\mu_s z)[1 - \exp(-\mu_s z)]}{1 + \omega_S^2 / \omega_H^2} + [1 - \exp(-\mu_s z)]^2 \frac{\omega_H^2}{\omega_S^2} \right\} \quad (1)$$

where $\langle i^2(z) \rangle$ is the mean square of the heterodyne signal current; α , the power to current conversion ratio; P_R and P_S , the power of the reference and input sample beams; σ_b , the effective backscattering cross-section; and ω_H and ω_S , the $1/e$ irradiance radius at the probing depth in the absence and presence of scattering, respectively. Pixels near the interface were excluded from the fit that was due to the specular reflection between the scattering and non-scattering media [18]. Besides, the profiles of averaged phase retardation signals have three layers (black arrows in the right column of Fig. 1), Δn could be calculated by linear least-squares fitting through the averaged Φ data over the depth of the ROI and then determined its slope from the following formula: $\Phi = (360/2\pi) \cdot k_0 \cdot d \cdot \Delta n$, where k_0 is the wave vector; d is the thickness of the fitting range. In addition, the mean fast-axis angle calculated by averaging across the width of the ROI at each depth could be determined from the following formula: $\beta = 1/2(180 - \Delta\phi)$, where $\Delta\phi$ is the phase difference of the oscillating P- and S-wave heterodyne signals.

Following PS-OCT imaging and quantitative optical properties extraction, all the specimens were fixed in 10% neutral formalin for 24 hours and then processed for standard paraffin embedding. Serial sections with 4 μ m thickness were cut within the region of the PS-OCT examination, and stained with hematoxylin and eosin (H and E) for routine examination. The distribution of collagen structure in the plaque lesion was also examined using a polarization microscope after picrosirius red staining. Finally, entire specimens were classified into normal vessel (N), lipid (L), fibrocalcific (C), and fibrous lesion (F) by a pathologist (J. J. Shyu).

Statistical analyses were performed using SPSS (version 14.0; SPSS Inc.). A p-value < 0.05 was considered to be statistically significant. The test of significant difference of optical

parameters by Kruskal-Wallis statistics was used to evaluate whether the four optical properties contributed to the differentiation between different kinds of vessels. After obtaining a significant test, multiple comparison procedures were then used to determine which means are different based on the equation,

$$|R_i - R_j| > Z_{\alpha/k(k-1)} \times \sqrt{\frac{n_i(n_i+1)}{12}} \times \left(\frac{1}{n_i} + \frac{1}{n_j} \right) \quad (2)$$

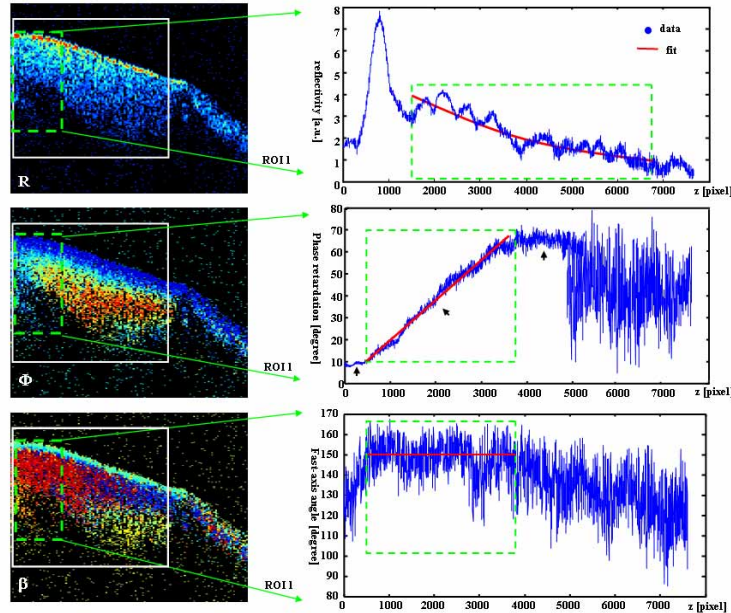


Fig. 1. Procedure of the PS-OCT extraction algorithm.

where R_i is the mean rank of the i th group , R_j is the mean rank of the j th group , k is the number of independent variables , n_t is the total numbers of sample , n_i and n_j represent the sample numbers of the i th and the j th group , $Z_{\alpha/k(k-1)}$ is the critical value at the significance level α and the $k(k-1)$ number of comparisons. A Spearman's ρ correlation test was also used to evaluate whether these four properties have correlations to each other.

Finally, multinomial logistic regressions were used to generate a predictive model based on a linear combination of weights ($X_{r\rho}$) of optical property (ρ =scattering coefficient, effective anisotropy factor, birefringence, and fast-axis angle) as in this equation:

$$\text{logit}\left[\frac{OR(\text{diseased vessel type})}{OR(\text{Normal vessel})}\right] = A_r + \sum B_{r\rho} X_{r\rho} \quad (3)$$

where OR = Odds Ratio, $r = \frac{C}{N}, \frac{F}{N}, \frac{L}{N}$, A_r is a constant, and $B_{r\rho}$ is an adjustable coefficient for each optical property. This model was then used to classify the artery specimens into four diagnostic classes. The accuracy of this model for plaque characterization was evaluated using Receiver Operating Characteristic (ROC) analysis [19]. The following statistics can be defined:

$$\text{Accuracy} = \frac{\text{TP} + \text{TN}}{\text{TP} + \text{TN} + \text{FP} + \text{FN}} \quad (4)$$

$$\text{Sensitivity} = \frac{\text{TP}}{\text{TP} + \text{FN}} \quad (5)$$

$$\text{Specificity} = \frac{\text{TN}}{\text{TN} + \text{FP}} \quad (6)$$

where the different fractions (TP, FP, TN, FN) represent true positive, false positive, true negative, and false negative, respectively.

3. Results

Figure 2 shows illustrative PS-OCT images with the corresponding histopathology of normal, lipid, fibroatheroma, and fibrocalcific plaques. Altogether, 135 ROIs from each regions in total R, Φ , and β images were collected. The extracted data, μ_s , g_{eff} , Δn , and β , are summarized in Fig. 3, where each box shows the median, 25th and 75th percentiles, and extreme values within a category. Open circles and stars indicate outlier data.

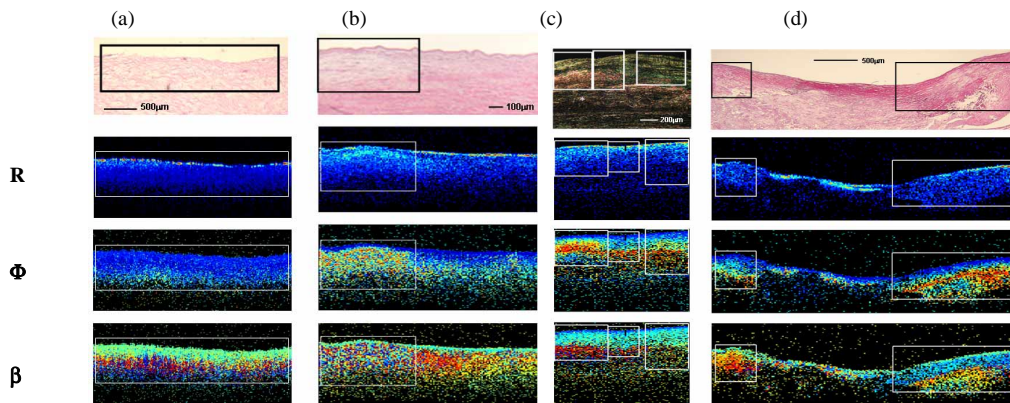


Fig. 2. Histological and PS-OCT images of (a) normal intima, (b) lipid lesion, (c) fibrous, and (d) fibrocalcific plaques.

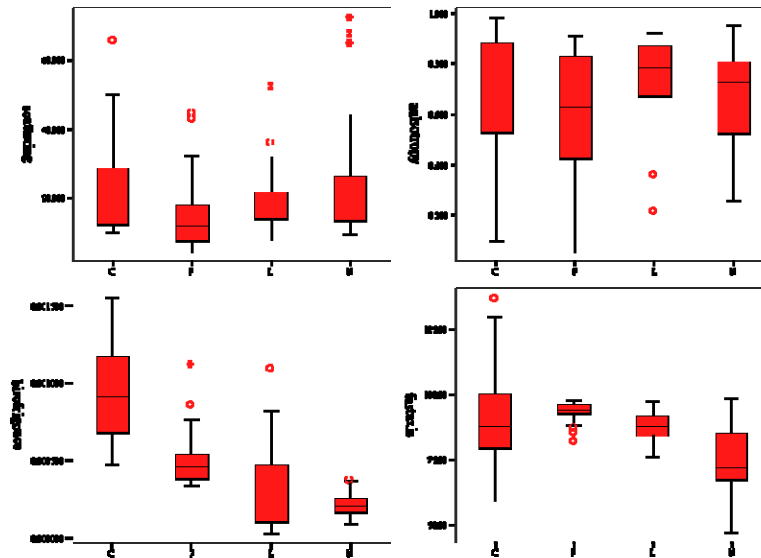


Fig. 3. Distributions of μ_s , g_{eff} , Δn , and β in normal vascular intima (N), lipid laden (L), fibrous (F), and fibrocalcific (C) plaques.

Kruskal-Wallis statistics (Table 1) shows that μ_s ($p = 0.022$), Δn ($p < 0.001$), and β ($p < 0.001$), have significant differences in normal vessels and three types of atherosclerotic vessels, by measuring how much the four group ranks differ from the mean rank (Table 2) of all groups. The g_{eff} value does not show any significant difference ($p=0.104$). From the multiple comparison test (Table 3), we found that F to C shows significant difference in μ_s ; Δn between C and N, F and N, L and C, L and F represent significant differences; and, β between C and N, F and N, L and N, L and F have significant difference.

Spearman's ρ correlation test shows that g_{eff} correlates to scattering coefficient ($r = -0.584$, $p = 0.003$) in fibrocalcific plaque, while this value correlates with birefringence value ($r = -0.563$, $p = 0.008$) in fibrous lesions. There are no other correlations. Finally, three regression models, Eqs. (9)-(11), were generated to predict the odds ratio of C to N, F to N, and L to N respectively.

$$\text{logit} \left[\frac{OR(\text{type} = C)}{OR(\text{type} = N)} \right] = -19.182 + 0.044X_{\mu_s} + 0.119X_{\Delta n} + 0.141X_{\beta} \quad (9)$$

$$\text{logit} \left[\frac{OR(\text{type} = F)}{OR(\text{type} = N)} \right] = -19.377 - 0.047X_{\mu_s} + 0.068X_{\Delta n} + 0.201X_{\beta} \quad (10)$$

$$\text{logit} \left[\frac{OR(\text{type} = L)}{OR(\text{type} = N)} \right] = -9.746 - 0.008X_{\mu_s} + 0.028X_{\Delta n} + 0.113X_{\beta} \quad (11)$$

Prediction results are given in Table 4. This method identified 17 of 23 lesions are fibrocalcific and 105 of 112 are not fibrocalcific. For fibrous plaque, the method identified 7 of 21 lesions are fibrous and 110 of 114 are not fibrous lesions. Finally, the method identified 33 of 48 lesions with lipid regions and 55 of 87 without lipid regions. Compared to the Intercept Only (Null model), where all parameters of that effect are zero, this model gives adequate predictions ($p < 0.001$). Accuracy, sensitivity, and specificity for the various characteristics are calculated and shown in Table 5.

Table 1 Kruskal Wallis Test Statistics

	μ_s	g_{eff}	Δn	β
Chi-Square	9.658	6.162	68.745	40.102
df	3	3	3	3
Asymp. Sig.	0.022	0.104	<0.001	<0.001

Table 2 Mean Ranks of four optical properties extracted from the four vessel types.

	N	C	F	L
μ_s	71.58	77.70	44.33	70.50
g_{eff}	62.79	70.72	54.36	77.33
Δn	45.57	119.09	92.48	52.91
β	40.37	75.39	102.90	73.94

Table 3 Multiple comparison test

μ_s	Type	N	C	F	L	Δn	Type	N	C	F	L	β	Type	N	C	F	L
	N						N		✓	✓			N		✓	✓	✓
	C			✓			C	✓			✓		C	✓			
	F		✓				F	✓			✓		F	✓			✓
	L						L		✓	✓			L	✓		✓	

Table 4 Plaque characterization by quantitative PS-OCT and histology

Classification				
Histology observed	Model predicted			
	N	C	F	L
N	27	0	0	16
C	1	17	2	3
F	0	1	7	13
L	7	6	2	33

Table 5 Quantitative plaque characterization of PS-OCT determined by histology

	C	F	L
Accuracy (%)	90	87	65
Sensitivity (%)	73.91 (51.6-89.7)*	33.33 (14.6-57)*	68.75 (53.7-81.3)*
Specificity (%)	93.75 (87.5-97.4)*	96.49 (91.3-99)*	63.22 (52.2-73.3)*

(* 95% confidence interval)

4. Discussion

In 2004, the first quantitative analysis of the optical scattering properties from OCT images of the normal and diseased human aortic intima in vitro at 1300 nm was proposed [18]. Their data suggested that very similar scattering properties were observed in normal samples but not in those atherosclerotic lesions. While in this study, we assessed arterial characteristics in human atherosclerosis vessels by extracting both scattering and birefringence properties from PS-OCT images. We further analyzed the significant difference of these quantified optical properties in different types of human vessels by using statistical methods.

Our preliminary data indicated that more than 80% normal arterial samples had μ_s between 10 and 39 mm^{-1} and have significant differences from other different types of plaques ($p < 0.05$), which is consistent with results obtained by Levitz, et. al [18]. From the multiple comparison tests, we also noticed that the significant difference in scattering property exists between fibrous and fibrocalcific plaques (i.e. marked in Table 3). These findings are consistent with results obtained with qualitative image-based plaque characterization methods where fibrous and fibrocalcific plaques can be distinguished by the signal-rich versus signal poor region [5, 7]. However, the effective anisotropy factor demonstrates no significant difference between normal and other atherosclerotic lesions (Table 1, $p = 0.104$), perhaps because the g_{eff} of the fibrocalcific and fibrous lesions were correlated with the μ_s and Δn properties, respectively. In relation to the birefringence property of the vessel that has not yet been quantitatively analyzed before. β values in the most atherosclerotic lesion were over 70 degrees, whereas smaller β values were presented in most fit areas of normal vascular intima. The Δn values were small and more concentrated in normal intima, but demonstrated larger

variations in the entire atherosclerotic lesion. The birefringence coefficient was larger in abundant thicker collagen fibers ($\Delta n = 9.409 \times 10^{-4}$; bright yellow to orange color, constituting > 60% of the left region in Fig. 2(c) histology) than in thin collagen fiber [$\Delta n = 5.386 \times 10^{-4}$; green color in right region of histology in Fig. 2(c)]. Both β and Δn values have significant differences between normal arterial vessel and other different types of plaques ($p < 0.05$).

In this study, the constructed regression model achieved 90%, 87%, and 65% prediction accuracy for C, F, and L, respectively. A high specificity (94% and 96% respectively) for diagnosing fibrocalcific and fibrous plaques in this quantitative PS-OCT criterion are comparable to that in the objective OCT image criteria (97% and 97% to 98%, respectively) [5]. However, false-negative PS-OCT diagnoses of fibrous plaques, lesions interpreted as fibrous plaque by histology, were perceived as lipid by the prediction model, resulting in a relatively low sensitivity of the quantitative PS-OCT criteria for diagnosing fibrous plaques (Table 5, 33%). The sources of discrepancy between quantitative PS-OCT and histological diagnosis could be attributed to the fewer specimens in this type of vessel, whereas several of these specimens come from the same person. The patient-specific effect of cluster data was not mentioned in other previous reports, and it will be considered in our further study. On the other hand, false-positive diagnoses of lipid lesions, perceived as lipid lesions by our prediction model, were mostly interpreted as normal vessels and partly interpreted as fibrous plaques by histology, resulting in a relatively low specificity of the quantitative PS-OCT criteria for diagnosing lipid plaques (Table 5, 63%). In this study, there was no attempt to differentiate a necrotic core from a lipid pool. Because the signal from the necrotic cores may be too weak for reliable measurements, future studies based on histological stains that can differentiate the two are needed. Also noteworthy is that Φ and β signals distributed in a slightly more random manner in the lipid lesion [Fig. 2(b)] than that in normal vessel wall [Fig. 2(a)], fibrous [Fig. 2(c)], and fibrocalcific plaque [Fig. 2(d)]. This may be due to the polarization state of light to be randomized by multiple scattering in lipid rich tissue, thus decrease the accuracy of birefringence measurement. Alternatively, further modifications of these PS-OCT criteria, such as the addition of threshold limit for the signal-poor region and the considering of the standard deviation of the birefringence signal within one ROI, may be needed to better differentiate lipid lesions.

Comparing to the objective OCT image criteria that have been substantially utilized by a number of research groups, OCT images of fibrous plaques were characterized by homogeneous, signal-rich regions; fibrocalcific plaques by well-delineated, signal-poor regions with sharp border; and lipid-rich plaques by signal-poor regions with diffuse borders. A high false positive rate for diagnosing fibrous caps was reported and it could be attributed to the difficulty in identifying plaques with diffuse border [7]. The validation of these criteria is obtained by two OCT training readers [5], whereas our computer-based quantitative analysis can determine plaque type automatically that eliminate the training time for each readers and the different diagnosis between interobserver. The quantitative information on both arterial scattering and birefringence properties can also be integrated with the qualitative visual information provided by PS-OCT images that will be supportive for facilitating image-based plaque characterization method.

5. Conclusion

This is the first study to predict the condition of the vessel by constructing of regression models from both scattering and birefringence properties of a vessel specimen. This is also the first time to assess the accuracy of quantitative PS-OCT for diagnosing plaque types. The results support efforts to develop a quantitative plaque characterization criterion, which could be a convenient complement to facilitate qualitative image-based plaque characterization methods. In the future, an analysis from a much larger set of specimens and the analysis considering of the effect of cluster data (i.e. specimens come from the same person) will be obtained for developing a more suitable prediction model. Moreover, it is likely that the combination of additional indexes (ex. presence of necrotic core, cap thickness, and

macrophage content) will have a greater predictive value for constructing a risk-stratifying plaque characterization criterion which could hold considerable promise for future clinical utility.

Acknowledgments

The authors thank the faculty and staff of the Department of Surgery of National Taiwan University Hospital for providing aortic specimens. They also thank the Biostatistics Laboratory, College of Public Health and Centre of Biostatistics Consultation, College of Public Health in National Taiwan University for their kindly help. This research was supported in part by the National Science Council of Taiwan (NSC 96-2628-M-003-001).